Scale heights and equivalent widths of the iron K-shell lines in the Galactic diffuse X-ray emission

Shigeo YAMAUCHI[1*], Kumiko K. NOBUKAWA[2], Masayoshi NOBUKAWA[3], Hideki UCHIYAMA[4], and Katsuji KOYAMA[2, 5]

[1]Department of Physics, Nara Women's University, Kitauoyanishimachi, Nara 630-8506

[2]Department of Physics, Graduate School of Science, Kyoto University, Kitashirakawa-oiwake-cho, Sakyo-ku, Kyoto 606-8502

[3]Department of Teacher Training and School Education, Nara University of Education, Takabatake-cho, Nara 630-8528

[4]Faculty of Education, Shizuoka University, 836 Ohya, Suruga-ku, Shizuoka 422-8529

[5]Department of Earth and Space Science, Graduate School of Science, Osaka University, 1-1 Machikaneyama-cho, Toyonaka, Osaka 560-0043

*E-mail: yamauchi@cc.nara-wu.ac.jp

Received ; Accepted

Abstract

This paper reports the analysis of the X-ray spectra of the Galactic diffuse X-ray emission (GDXE) in the Suzaku archive. The fluxes of the Fe I Kα (6.4 keV), Fe XXV Heα (6.7 keV) and Fe XXVI Lyα (6.97 keV) lines are separately determined. From the latitude distributions, we confirm that the GDXE is decomposed into the Galactic center (GCXE), the Galactic bulge (GBXE) and the Galactic ridge (GRXE) X-ray emissions. The scale heights (SHs) of the Fe XXV Heα line of the GCXE, GBXE and GRXE are determined to be $\sim$40, $\sim$310 and $\sim$140 pc, while those of the Fe I Kα line are $\sim$30, $\sim$160 and $\sim$70 pc, respectively. The mean equivalent widths (EWs) of the sum of the Fe XXV Heα and Fe XXVI Lyα lines are $\sim$750 eV, $\sim$600 eV and $\sim$550 eV, while those of the Fe I Kα line are $\sim$150 eV, $\sim$60 eV and $\sim$100 eV for the GCXE, GBXE and GRXE, respectively. The origin of the GBXE, GRXE and GCXE is separately discussed based on the new results of the SHs and EWs, in comparison with those of the Cataclysmic Variables (CVs), Active Binaries (ABs) and Coronal Active stars (CAs).

Key words: Galaxy: disk — X-rays: diffuse background — X-rays: ISM

1 Introduction

The Galactic diffuse X-ray emission (GDXE) is unresolved X-ray emission along the Galactic plane (Worrall et al. 1982; Warwick et al. 1985). Strong K-shell lines from highly ionized atoms were found in the GDXE spectra (Koyama et al. 1986; Koyama et al. 1989; Yamauchi et al. 1990; Yamauchi & Koyama 1993; Kaneda et al. 1997; Sugizaki et al. 2001; Ebisawa et al. 2005). Subsequently, the K-shell lines were resolved into Helium-like and Hydrogen-like atomic lines, such as Fe XXV Heα, Fe XXVI Lyα, S XV Heα and S XVI Lyα (Koyama et al. 1996; Koyama et al. 2007b; Ebisawa et al. 2008; Heard & Warwick 2013a). The Fe XXV Heα (6.7 keV) and Fe XXVI Lyα (6.97 keV) lines are emitted from a high temperature plasma (HP) of kT ~5–7 keV, while the S XV Heα (2.46 keV) and S XVI Lyα (2.62 keV) lines come from a low temperature plasma (LP) of kT ~1 keV. Koyama et al. (1996) discovered Fe I Kα (6.4 keV) lines from the Galactic center (GC) region. Bright regions are associated with molecular clouds, hence the origin is fluorescence from cool gas (CG). They are called as the X-ray reflection nebulae (XRNe). Furthermore, Ebisawa et al. (2008) and Yamauchi et al. (2009) found the Fe I Kα line in the various regions along the Galactic plane. Therefore the Fe I Kα line emission is not only from XRNe, but its large fraction is more extended emission along Galactic plane. From the spatial distributions of the Fe K-shell lines, Koyama et al. (1989), Yamauchi & Koyama (1993) and Uchiyama et al. (2013) decomposed the GDXE into the Galactic Center (GCXE), Galactic Bulge (GBXE) and Galactic Ridge (GRXE) X-ray Emissions

Long standing debates have been the origin of the GDXE. Most of the previous debates were based on the observations of limited spatial and spectral resolution, where the GDXE was not separated into the GRXE, GBXE and GCXE. The K-shell line emission at ~6.7 keV was not resolved to the Fe I Kα, Fe XXV Heα and Fe XXVI Lyα lines.

In this paper, we analyze the Suzaku archive data from a large number of pointing positions along the inner Galactic plane. We confirm that the GDXE is composed of the GCXE, GBXE and GRXE. Furthermore we separately determine the scale heights (SHs) and equivalent widths (EWs) of the Fe I Kα, Fe XXV Heα and Fe XXVI Lyα lines in the GCXE, GBXE and GRXE. Based on these results, we examine the origin of the HP and CG in the GCXE, GBXE and GRXE. Throughout this paper, the distance to the GC is 8 kpc and quoted errors are in the 68% (1σ) confidence limits.

2 Observations and Data Reductions

Suzaku observations of the GDXE were carried out with the X-ray Imaging Spectrometers (XIS, Koyama et al. 2007a) placed at the focal planes of the thin-foil X-ray Telescopes (XRT, Serlemitsos et al. 2007). The XIS consisted of 4 sensors: XIS sensor-1 (XIS1) had a back-illuminated CCD (BI), while the other three XIS sensors (XIS0, 2, and 3) had front-illuminated CCDs (FI). Since XIS 2 turned dysfunctional on 2006 November 9, the other three sensors (XIS 0, 1, and 3) were operated after the epoch. A small fraction of the XIS 0 area was not used since 2009 June 23 because of the damage by a possible micro-meteorite. The XIS was operated in the normal clocking mode. The field of view (FOV) of the XIS was $17'.8 \times 17'.8$.

We selected the data set near the Galactic plane from all the Archive Suzaku data, where no bright X-ray source was included. The number of the data set (pointing positions) was 143, about 2.3 times larger than that of the previous work by Uchiyama et al. (2013). The pointing positions (Galactic coordinates) and exposure times are listed in table 1.

Data reduction and analysis were made using the HEASOFT. The XIS pulse-height data for each X-ray event were converted to Pulse Invariant (PI) channels using the `xispi` software and the calibration database. We excluded the data obtained at the South Atlantic Anomaly, during Earth occultation, and at low elevation angles from the Earth rim of $< 5^\circ$ (night Earth) or $< 20^\circ$ (day Earth). After removing hot and flickering pixels, we used the grade 0, 2, 3, 4, and 6 data.

3 Analysis and Resluts

3.1 Derivations of the Fe I Kα, Fe XXV Heα and Fe XXVI Lyα fluxes

We extracted X-ray photons from the entire region of the XIS FOV, excluding discrete sources in the FOV and the calibration sources located at the corners of the XIS sensors. In order to achieve the highest signal-to-noise ratio in the Fe band, we used only the FI detectors because the sensitivity in the Fe band was better than that of the BI detector (Koyama et al. 2007a). To maximize the photon statistics, data of each XIS sensor were merged. The response files, Redistribution Matrix Files (RMFs) and Ancillary Response Files (ARFs), were made for each data set using `xisrmfgen` and `xissimarfgen` of the HEASOFT package, respectively. The non-X-ray background (NXB) was constructed from the night earth data provided by the XIS team using `xisnxbgen` of the HEASOFT package (Tawa et al. 2008).

We made an X-ray spectrum in the 4–10 keV band from each position. After the subtraction of

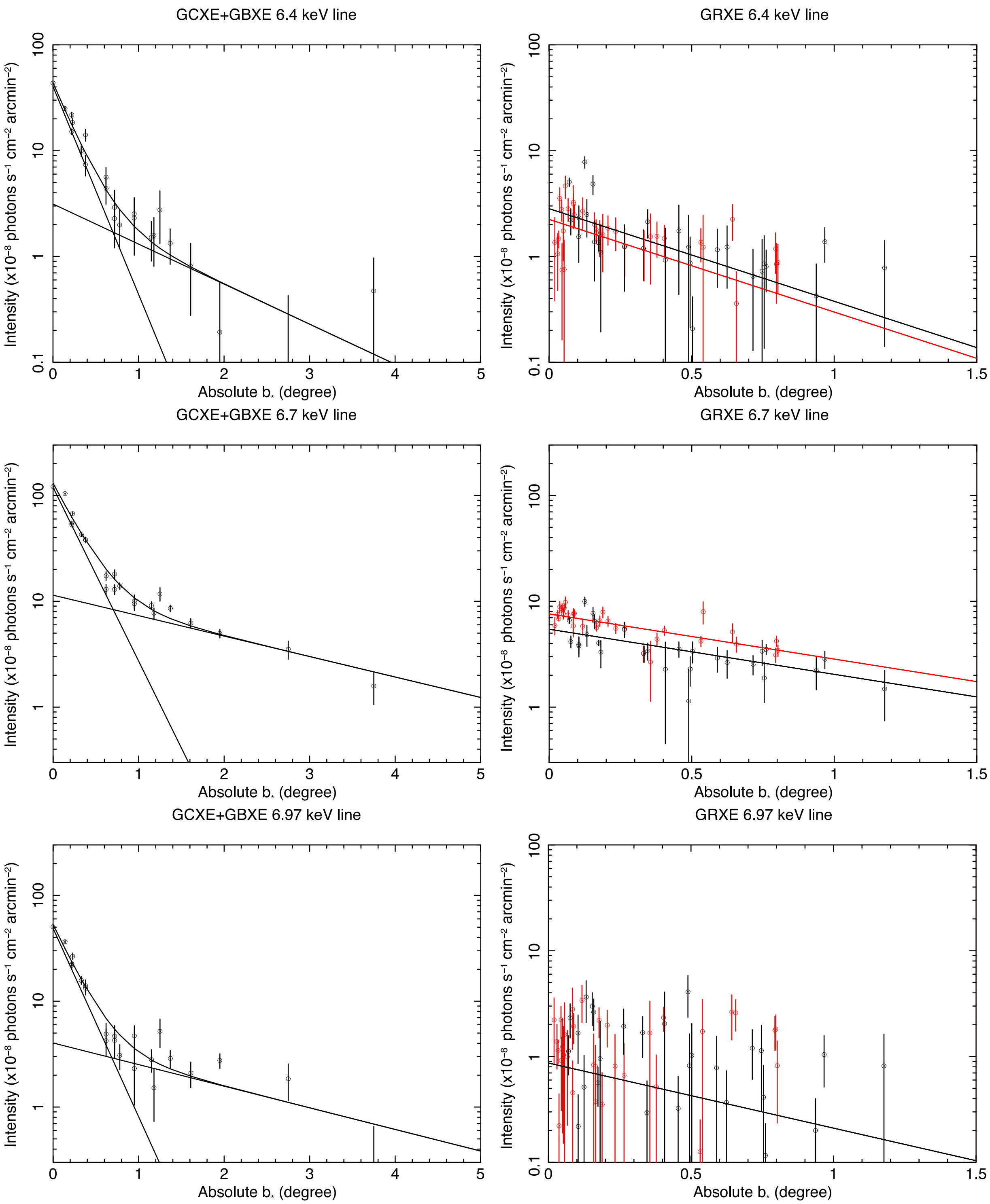

Fig. 1. Galactic latitude distribution of the Fe I Kα (6.4 keV) (top), Fe XXV Heα (6.7 keV) (middle) and Fe XXVI Lyα (6.97 keV) (bottom) line fluxes. Left: region (a) data of $|l| < 0.^{\circ}5$. The black lines show the best-fit model for the GCXE and GBXE. Right: region (d) data from l=10°–30° (red) and l=330°–350° (black). The black and the red lines show the best-fit model.

the NXB, we fitted the spectra with a phenomenological model: a power-law plus a bremsstrahlung and many Gaussian lines. The power-law is the cosmic X-ray background (CXB) with the fixed photon index (Γ) and flux of 1.4 and 10 photons s^{-1} cm^{-2} sr^{-1} keV^{-1} at 1 keV, respectively (Marshall et al. 1980; Gendreau et al. 1995; Kushino et al. 2002; Revnivtsev et al. 2005). The bremsstrahlung and Gaussian lines are for the GDXE model.

We assumed the absorption column for the GC regions of $|l| \leq 5^\circ$ and $|b| \leq 0^\circ\!.5$, $N_{\rm H}$(GCXE), to be 6×10^{22} cm^{-2} (Sakano et al. 2002). For the GRXE and GBXE regions of $|b| \leq 1^\circ$ and $|b| \geq 1^\circ$, $N_{\rm H}$(GRXE) and $N_{\rm H}$(GBXE) were fixed to 3×10^{22} cm^{-2} and 1×10^{22} cm^{-2}, respectively. We note that the assumed $N_{\rm H}$ has no large effect in the energy band of 5–8 keV. The absorption of the CXB, $N_{\rm H}$(CXB), was assumed to be twice of the interstellar absorption of $N_{\rm H}$(GDXE). The cross section of photoelectric absorption was taken from Balucinska-Church and McCammon (1992). As noted in Koyama et al. (2007b), in the GDXE spectrum, a clear absorption edge of neutral or lower ionized iron was found at 7.1 keV. Therefore we set the Fe abundance of the absorption column as a free parameter if the spectra exhibited a deep absorption edge.

The temperature and the normalization of the bremsstrahlung were free parameters. The fluxes of the Fe I Kα (6.4 keV), Fe XXV Heα (6.7 keV) and Fe XXVI Lyα (6.97 keV) lines were also free parameters, but the flux of the Fe I Kβ line at 7.058 keV was fixed to the theoretical value of 0.125 times Fe I Kα (Kaastra & Mewe 1993). Since the Fe XXV Heα line was a blend of the resonance, intercombination and forbidden lines, the intrinsic line width of Fe XXV Heα was assumed to be 23 eV (Koyama et al. 2007b). Emission lines of Ni I Kα (7.49 keV), Ni XXVII Heα (7.77 keV), Fe XXV Heβ (7.88 keV), Fe XXVI Lyβ (8.25 keV), Fe XXV Heγ (8.29 keV) and Fe XXVI Lyγ (8.70 keV) were added if the spectra had high statistics.

3.2 Scale height

In order to investigate the latitude distribution of the Fe I Kα, Fe XXV Heα and Fe XXVI Lyα lines, and the 5–8 keV band flux, the best-fit results were grouped into the 4 regions: (a) $|l| < 0^\circ\!.5$, (b) l=358$^\circ\!.5$, (c) l=356$^\circ\!.0$–356$^\circ\!.4$ and (d) $|l|$=10°–30°. Here and after, we used a new Galactic coordinate of (l_*, b_*)= ($l + 0^\circ\!.056$, $b + 0^\circ\!.046$), referring the GC (Sgr A*) position of (l, b)=($-0^\circ\!.056$, $-0^\circ\!.046$).

The latitude profiles of the Fe I Kα, Fe XXV Heα and Fe XXVI Lyα lines in the regions (a) and (d) are given in figure 1. The left panels clearly show an existence of two components, while the right panels show a single component. The region (a) is mainly the GCXE data with a small fraction of the GBXE, while the regions (b) and (c) are vice versa. The region (d) is the data of the pure GRXE (Yamauchi & Koyama 1993; Uchiyama et al. 2013).

We simultaneously fitted the profiles of (a), (b) and (c) with a two-exponential model of

$$I(b_*) = A_{\rm GCXE} \exp(-\frac{|b_*|}{b_{\rm GCXE}}) + A_{\rm GBXE} \exp(-\frac{|b_*|}{b_{\rm GBXE}}), \qquad (1)$$

where $b_{\rm GCXE}$ and $b_{\rm GBXE}$ are e-folding scales (degree) of the GCXE and GBXE, respectively and $A_{\rm GCXE}$ and $A_{\rm GBXE}$ are normalizations of the GCXE and GBXE, respectively. We linked $b_{\rm GCXE}$ and $b_{\rm GBXE}$ of (a), (b) and (c) each other and scaled $A_{\rm GCXE}$ of (b) and (c) to (a) using the e-folding longitude scale of the GCXE of $0\overset{\circ}{.}63$ (Uchiyama et al. 2013).

The data of (d) were fitted with a one-exponential model of

$$I(b_*) = A_{\rm GRXE} \exp(-\frac{|b_*|}{b_{\rm GRXE}}), \qquad (2)$$

where $b_{\rm GRXE}$ and $A_{\rm GRXE}$ are the e-folding scale (degree) and normalization of the GRXE, respectively. We excluded the local enhanced regions, the XRNe and bright supernova remnant (SNR) Sgr A East in the GCXE (e.g., Koyama et al. 1996; Park et al. 2004).

The best-fit parameters are listed in table 2. The e-folding scales in table 2 are essentially the same as those derived by Uchiyama et al. (2013), except for the e-folding latitude scale of the GRXE. This disagreement was due to the data set selection; Uchiyama et al. (2013) used the data mainly near the GCXE, and hence the e-folding scale of the GRXE was largely affected by the large value of the GBXE (see table 2). Our estimate of the GRXE was based on a lot of pure GRXE results in the range of $|l| = 10°$–$30°$, and hence would be more reliable. On the other hand, the e-folding longitude scale for the GCXE and GRXE by Uchiyama et al. (2013) would be reliable due to limited contribution of the GBXE. Assuming the distance of 8 kpc, the e-folding scales (degree) of the latitude distribution in the 6-th column of table 2 were converted to the SHs (pc). The results are listed in the last column in table 2.

3.3 Equivalent width

Figure 2 show the longitude profiles of the line flux of Fe I Kα, Fe XXV Heα and Fe XXVI Lyα, and those of the flux ratios of Fe I Kα/Fe XXV Heα and Fe XXVI Lyα/Fe XXV Heα. The longitude distribution of the Fe XXV Heα and Fe XXVI Lyα lines are symmetry with respect to the Galactic center. However the Fe I Kα flux and the flux ratio relative to the Fe XXV Heα line (Fe I Kα/Fe XXV Heα) show east-west asymmetry at l=$1\overset{\circ}{.}5$–$3\overset{\circ}{.}5$ and l= 330°–340° regions (see figure 2, the 1-st and 4-th panels).

We obtained the EWs of the Fe I Kα (EW$_{6.4}$), Fe XXV Heα (EW$_{6.7}$) and Fe XXVI Lyα (EW$_{6.97}$) lines from the positions of the GCXE ($|l|$ <$1\overset{\circ}{.}5$, $|b|$ ≤$0\overset{\circ}{.}5$), GBXE ($|l|$ <$4\overset{\circ}{.}0$, $|b|$ ≥$1\overset{\circ}{.}0$) and GRXE ($|l|$=10°–30°, $|b|$ ≤$1\overset{\circ}{.}0$), where the local enhancements due to XRNe and the supernova remnant

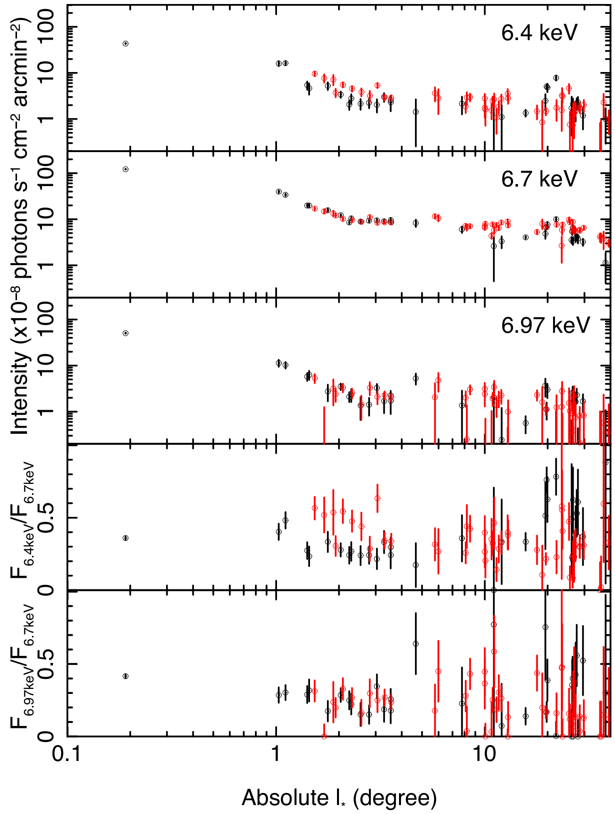

Fig. 2. Galactic longitude distribution of the Fe I Kα, Fe XXV Heα and Fe XXVI Lyα line fluxes, and the flux ratios of Fe I Kα/Fe XXV Heα and Fe XXVI Lyα/Fe XXV Heα. Referring the e-folding scale of the GCXE and GRXE (table 2), we select the data of $|b_*| < 0.^\circ 2$ and $|b_*| < 0.^\circ 5$ in the regions of $|l_*| < 1.^\circ 5$ (GCXE) and $|l_*| > 1.^\circ 5$ (GRXE), respectively. The data containing the XRNe and Sgr A East SNR are excluded. The red and black colors show the data of $l_* > 0^\circ$ and $l_* < 0^\circ$, respectively.

(SNR) Sgr A East in the GCXE were excluded.

The EW$_{6.4}$, EW$_{6.7}$ and EW$_{6.97}$ relations of the GCXE are plotted in figure 3a and 3b. Although the EW$_{6.4}$ and EW$_{6.7}$ show no clear correlation (a correlation coefficient, R$\sim$0.1), the EW$_{6.97}$ and EW$_{6.7}$ show a correlation (R$\sim$0.6). The best-fit proportional line is plotted in figure 3b. The same plots of the EW$_{6.4}$ and EW$_{6.7}$ relations of the GBXE and GRXE are shown in figure 3c and 3d, respectively. We also made the EW$_{6.7}$ and EW$_{6.97}$ relation plots in the GBXE and GRXE. Due to the large statistical errors, we found no clear correlation in the GBXE and GRXE data (R~ -0.2 – 0.5).

For the GCXE, GBXE and GRXE, the mean EW$_{6.4}$ values were 145$\pm$3, 61$\pm$11 and 97$\pm$12 eV, the EW$_{6.7}$ were 527$\pm$4, 443$\pm$14 and 428$\pm$15 eV and the EW$_{6.97}$ were 221$\pm$3, 160$\pm$14 and 117$\pm$19 eV, respectively.

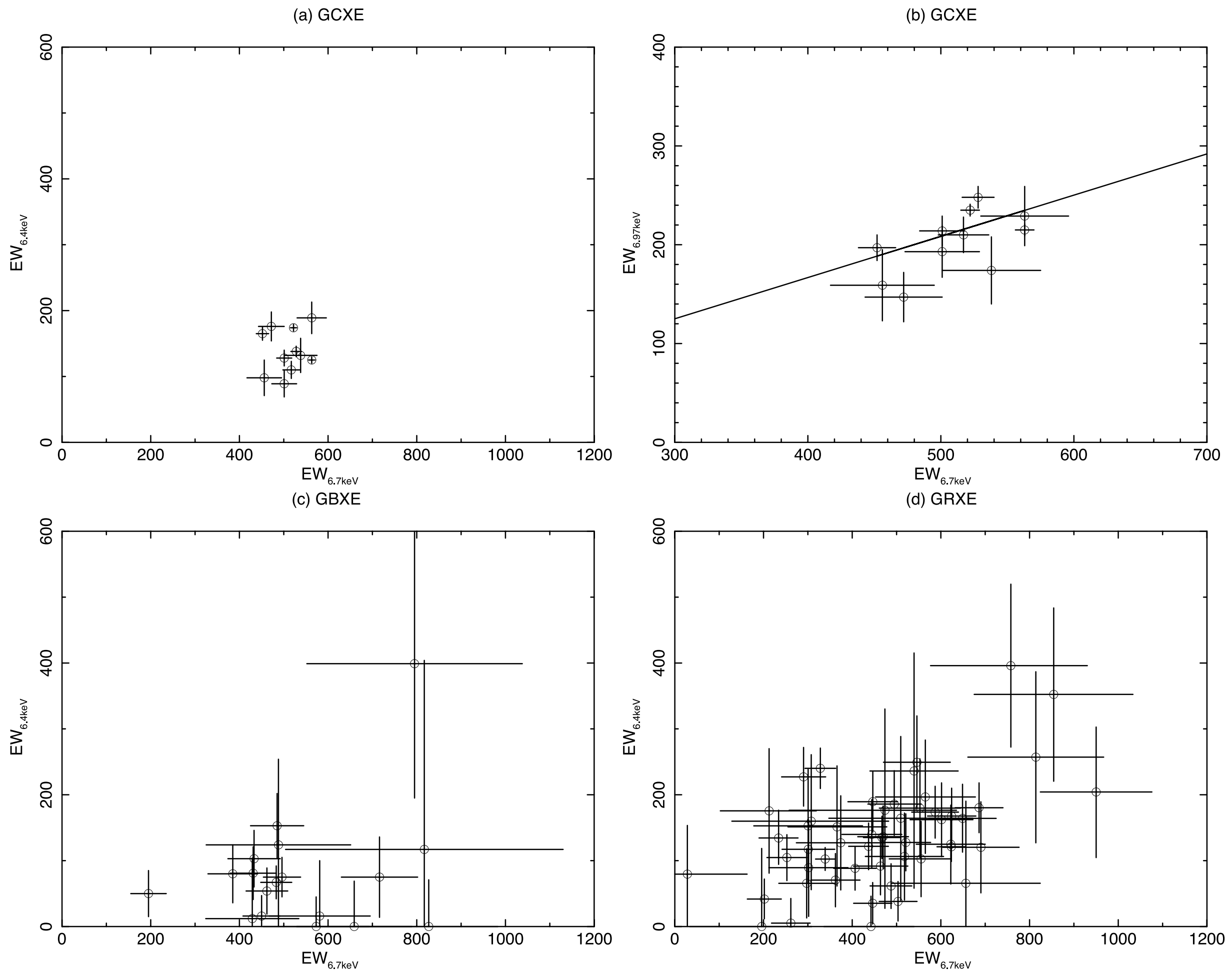

Fig. 3. (a) Correlation plot of the EWs of $EW_{6.4}$ and $EW_{6.7}$ in the GCXE. (b)the same as (a) but the correlation is $EW_{6.97}$ between $EW_{6.7}$. The solid line is the best-fit proportional line of $EW_{6.97}$= 0.42$\times$$EW_{6.7}$. (c) the same as (a) but in the GBXE. (d) the same as (a) but in the GRXE.

4 Discussion

4.1 Overview of the point source origin of the GDXE

Since the discovery of strong iron K-shell lines in the GDXE, the origin of the GDXE becomes a long standing question. One of the most accepted idea is the point source origin (Revnivtsev et al. 2006). The point source origin is based on the X-ray luminosity function (XLF) of the continuum flux (e.g., the 2–10 keV band). In the luminosity range of $\sim 10^{30}$–10^{33} erg s^{-1}, the XLF of point sources consists of mainly cataclysmic variables (CVs) and active binaries (ABs). It is made using the RXTE sky survey and the ROSAT all sky survey, where the ROSAT flux in the 0.1–2.4 keV band were converted to the 2–10 keV band. This conversion process causes a large systematic error of $\geq$50% (Sazonov et al. 2006). In the lower luminosity band 5×10^{27}–$\sim 10^{30}$ erg s^{-1}, the XLF mainly consists of coronal active stars (CAs), where the systematic error would be even larger (Sazonov et al. 2006).

Nevertheless, the strongest support on the point source origin at this time came from the deep observation with Chandra. Revnivtsev et al. (2009) resolved ~ 80% of the GDXE flux into point sources following the XLF of Sazonov et al. (2006). Although the authors did not compare the iron K-shell line fluxes (EW) with those of CVs and ABs, they regarded that major sources of the Fe I Kα, Fe XXV Heα and Fe XXVI Lyα lines are CVs and ABs following Sazonov et al. (2006) because these sources have been known as strong iron line emitters.

We have separately determined the EWs and SHs of the Fe I Kα, Fe XXV Heα and Fe XXVI Lyα lines in the GCXE, GBXE and GRXE. In the next subsections, we therefore re-examine the point source origin of the GCXE, GBXE and GRXE based on these new observational results of the EWs and SHs, in comparison with those of the published results of CVs, ABs and CAs. In the current point source origin, magnetized CVs (mCVs) cover the energy range of $\gtrsim 10^{32}$ erg s^{-1}. Non magnetized CVs (nmCVs), often called as dwarf novae, and bright ABs are in the range of $\sim 10^{30}$–10^{32} erg s^{-1}. The lowest luminosity band of $\lesssim 10^{31}$ erg s^{-1} is covered by faint ABs and CAs (e.g., Sazonov et al. 2006).

4.2 Iron line equivalent widths and scale heights of CVs, ABs and CAs

Since the EWs of Fe XXV Heα and Fe XXVI Lyα show a correlation (figure 3b), and the SHs of these lines are similar (table 2), the origin would be the same. We therefore sum $\mathrm{EW}_{6.7}$ and $\mathrm{EW}_{6.97}$ ($\mathrm{EW}_{6.7}$+$\mathrm{EW}_{6.97}$) hereafter. The mean $\mathrm{EW}_{6.4}$ and $\mathrm{EW}_{6.7}$+$\mathrm{EW}_{6.97}$ of mCVs are ~120 eV and ~260 eV, respectively (Ezuka & Ishida 1999; Hellier et al. 1998; Hellier & Mukai 2004; Bernardini et al. 2012; Eze 2015; Xu et al. 2016). There is significant variation of the observed mean EWs from the author to author. We checked the author-to-author variations and found to be ~40% at most. The same order of uncertainty would be exist in the following estimation of the mean EWs in the other point sources.

Since nmCVs have lower flux but about 10 times larger space density than mCVs (Patterson 1984), they would be important contributors to the GDXE in the energy range of $\sim 10^{30}$–10^{32} erg s^{-1}. Mukai & Shiokawa (1993) reported that the sum of $\mathrm{EW}_{6.4}$+$\mathrm{EW}_{6.7}$+$\mathrm{EW}_{6.97}$ was ~780 eV, where unreasonably large EW samples were excluded. Byckling et al. (2010) reported that $\mathrm{EW}_{6.4}$ was ~90 eV, while Rana et al. (2006) reported that $\mathrm{EW}_{6.4}$, $\mathrm{EW}_{6.7}$ and $\mathrm{EW}_{6.97}$ were ~60 eV, ~260 eV and ~85 eV, respectively. Xu et al. (2016) analyzed 16 samples in the Suzaku archive and found $\mathrm{EW}_{6.4}$ ~62 eV, $\mathrm{EW}_{6.7}$ ~438 eV and $\mathrm{EW}_{6.97}$ ~95 eV. Thus in average, $\mathrm{EW}_{6.4}$ and $\mathrm{EW}_{6.7}$+$\mathrm{EW}_{6.97}$ of nmCVs are ~70 eV and ~530 eV, respectively.

Schmitt et al. (1990) compiled the Einstein data of X-ray stars. The major sources are ABs and CAs in the luminosity range of $\sim 10^{30}$–10^{32} erg s^{-1} and 10^{27}–10^{30} erg s^{-1}, respectively. Since the spectral information of ABs in the iron K-shell band has been very limited so far, we estimate the EW from the observed Fe abundance and plasma temperature. The mean temperature and iron abundance are reported to be $\sim$3 keV, and $\sim$0.3 solar, respectively (Tsuru et al. 1989; Doyle et al. 1991; Dempsey et al. 1993; Antunes et al. 1994; White et al. 1994; Güdel et al. 1999; Osten et al. 2000; Audard et al. 2003; Pandey & Singh 2012), and hence the $EW_{6.4}$ is negligible, and the sum of $EW_{6.7}$ and $EW_{6.97}$ is estimated to be $\sim$650 eV. Recently, Xu et al. (2016) obtained $EW_{6.4} \leq$20 eV, $EW_{6.7} \sim$286 eV and $EW_{6.97} \sim$12 eV from the 4 Suzaku samples. Thus, $EW_{6.4}$ and $EW_{6.7}+EW_{6.97}$ of ABs are $\leq$20 eV and 300–650 eV, respectively. The 6.4 keV line would be due to irradiation of the stellar photosphere by the coronal hard X-rays.

The EWs of CAs are even more unclear, but may be an important component in the luminosity range of $\lesssim 10^{30}$ erg s^{-1} (Sazonov et al. 2006). Since X-rays from CAs are due to dynamo activity, young CAs in the pre-main sequence (PMS) and fast rotating CAs in an earlier phase are more active than old CAs in the main sequence (MS) (Güdel 2004). Pandey & Singh (2008) reported the temperature of a late type dwarf to be $\leq$ 1 keV. The temperature is too low to excite the iron K-shell lines, and hence old CAs would be ignored as the candidate of the GDXE origin. The young CAs (PMS) in the star forming regions of the ρ-Oph and the Orion nebula clouds have the X-ray luminosity and the mean temperature of 10^{28}–$10^{31.5}$ erg s^{-1} and 2–3 keV, respectively (Imanishi et al. 2003; Ozawa et al. 2005; Prisinzano et al. 2008). The Fe abundance is $\sim$0.2–0.4 solar. A fraction of young CAs in molecular clouds (MCs) show $EW_{6.4} \sim$100–400 eV (Takagi et al. 2002; Tsujimoto et al. 2005; Czesla & Schmitt 2010). Tsujimoto et al. (2005) concluded that the 6.4 keV line arises from reflection of circumstellar disks. However, these are very rare cases, and hence the mean EWs of young CAs may be more or less similar to the ABs. In order to help the re-examination of the point source origin, we list the EWs of the GDXE and candidate point sources in table 3.

The SHs of stars depend on the mass (e.g., Hawkins 1988; Gilmore & Zeilik 2000; Bimmey & Tremaine 2008): $\lesssim$100 pc for high-mass stars and $\gtrsim 100$ pc for low-mass stars. Then the SH of CVs (mCVs+nmCVs) are in the range of 130–160 pc (Patterson 1984; Ak et al. 2008; Revnivtsev et al. 2008). The spectral types of ABs are mostly G-K type with small fraction ($\sim$15%) of F type (Strassmeier et al. 1993). Then the SH of ABs is $\sim$150–300 pc, similar to those of G–K type stars (Gilmore & Zeilik 2000). The SH of CAs in the MS would be $\sim$150–300 pc. However the CAs with age of $\lesssim$10 Myrs, the CAs are not largely diffused out from the mother clouds, and hence the SH would be similar to MCs, $\lesssim$100 pc.

4.3 Galactic Bulge X-ray Emission (GBXE)

Revnivtsev et al. (2009) conducted a deep observation ($\sim$1 Msec) in the region of (l, b)=(0°.1, $-$1°.4) (Chandra Bulge Field, CBF). Although the CBF is near the GCXE region, the flux ratio of the iron K-shell lines of the GBXE and GCXE (GBXE/GCXE) are $\sim$10 (see figure 1 left at $|b_*|$ $\sim$1°.4). Thus the CBF can be regarded as almost a pure GBXE region. In the CBF, Revnivtsev et al. (2009) and Hong (2012) reported that $\sim$70–80% flux (6.5–7.1 keV band) in the central region was resolved into point sources. However it is very surprising that the profiles of the 6.5–7.1 keV flux as a function of 2–10 keV luminosity by Hong (2012) is $\sim$2 times larger than that of Revnivtsev et al. (2009) in the most important luminosity range of 10^{31}–10^{32} erg s^{-1}. Furtheremore, about 20% of the faintest point sources are unique in each point source lists. Hong (2012) argued following his luminosity function that the major component is mCVs in contrast to major point source origin scenarios.

Morihana et al. (2013), on the other hand, reported that $\sim$50% (2–8 keV band) of the full CBF field was resolved into point sources. In figure 13 of Morihana et al. (2013), EW$_{6.7}$ of the CBF is $\sim$100 eV in the luminosity range of $\gtrsim 10^{32}$ erg s^{-1}, where a candidate source may be mCVs. It constantly increases in the range of 7×10^{30}–7×10^{31} erg s^{-1}. This trend would be due to increasing contribution of nmCV and bright ABs, which is against the argument of Hong (2012). In the range of $\lesssim 7 \times 10^{30}$ erg s^{-1}, the EWs become nearly constant at $\sim$300 eV, where main contributors would be faint ABs, CAs and others.

We see many systematic errors and/or differences from author to author in the quantities of the point sources scenario even for the GBXE. These possible errors may be ignored in the luminosity range of $\gtrsim 10^{30}$ erg s^{-1}. Thus a robust conclusion may be that point sources occupy $\sim$50–70% of the total GBXE flux in the $\gtrsim 10^{30}$ erg s^{-1} range. The SH$_{6.7}$ and SH$_{6.97}$ of $\sim$310 pc and SH$_{6.4}$ of $\sim$160 pc are consistent with those of nmCVs and ABs. Also the EW$_{6.4}$ and EW$_{6.7}$+EW$_{6.97}$ are not inconsistent with the sum of nmCVs and ABs in any mixing ratio (table 3). Thus we suspect that some fraction ($\sim$10–20%) of the GBXE is mCVs, while a major fraction ($\sim$40–50%) are due to nmCVs and bright ABs, which covers mainly the luminosity range of 10^{30}–10^{32} erg s^{-1}. To explain another $\sim$ 30–50%, more reliable information of the spectra of faint nmCVs, ABs, CAs or other objects is necessary.

4.4 Galactic Ridge X-ray Emission (GRXE)

The SH$_{6.7}$ and SH$_{6.97}$ are $\sim$140 pc and $\sim$100 pc, respectively. Within the error of $\sim$20–40 pc, these may be marginally consistent with those of CVs and ABs. The EW$_{6.7}$+EW$_{6.97}$ of $\sim$550 eV is similar to the GBXE. Thus the origin of HP may be more or less similar to the GBXE: a large fraction is nmCVs+ABs in the luminosity range of $\lesssim 10^{32}$ erg s^{-1}. On the other hand, the EW$_{6.4}$ of $\sim$100 eV is

$\sim$1.5–3 times larger and $\mathrm{SH}_{6.4}$ of $\sim 70\pm20$ pc is smaller than any mixing ratio of mCVs, nmCvs and ABs. We therefore more seriously examine the origin of the Fe I Kα line than the case of the GBXE.

Large excesses of the Fe I Kα relative to the Fe XXV Heα line at l=1.°5–3.°5 and l=330°–340° (see figure 2) are also against the point source origin for the Fe I Kα line. Since the excess is nearly 2 times of the average level, a significant fraction should be in unknown components, which have strong Fe I Kα lines. The $\mathrm{SH}_{6.4} \sim 70\pm20$ pc is similar to the MC distribution (Mathis 2000; Stark & Lee 2005). Therefore the Fe I Kα line would mainly originate from MCs.

Molaro et al. (2014) claimed that $\sim$10–30% of the total luminosity of the GRXE would be the scattered flux of LMXBs. Using the best-fit parameters listed in table 2, the 5–8 keV band luminosity in the ($|l_*| = 10°$–$30°$, $|b_*| \leq 0.°5$) region is estimated to be $\sim 6\times10^{36}$ erg s^{-1}, while that of all the cataloged LMXBs in the same region is $\sim 7\times10^{37}$ erg s^{-1} (Liu et al. 2007). The line-of-sight (on-plane) N_{H} from this region is $\sim 4\times10^{22}$ cm^{-2} (e.g., Ebisawa et al. 2005; Yasumi et al. 2014). For simplicity, we assume a uniform density disk of 6 kpc radius and 70 pc thick around each LMXB, then N_{H} averaging 4π steradian around the LMXB is estimated to be $\sim 4\times10^{21}$ cm^{-2}. Therefore the Thomson scattered luminosity is $\sim 2\times10^{35}$ erg s^{-1}. This is a few % of the GRXE in this region, and hence we can safely conclude that the contribution of LMXBs to the Fe I Kα flux of the GRXE is minor fraction.

Another possible source of the Fe I Kα line is ionization by low-energy cosmic-rays (LECR), either protons (LECRp) or electrons (LECRe). Nobukawa et al. (2015) consistently explained that the Fe I Kα excess at l=1.°5–3.°5 is due to LECRp. In general, the most probable site of the LECRs is SNRs. However, our spectral data include no X-ray SNR. Also only a few SNRs are associated with the diffuse Fe I Kα line (Sato et al. 2014; Sato et al. 2015).

4.5 Galactic Center X-ray Emission (GCXE)

Since the EWs of the GCXE are much larger than the GBXE and GRXE, the major origin of the GCXE cannot be the same as the GBXE and GRXE, namely nmCVs and ABs. Uchiyama et al. (2011) found that the Fe XXV Heα line shows large excess over the stellar mass density model, assuming that all the GRXE and GBXE are due to integrated emission of point sources. The same excess over the real infrared star count profile is found by Yasui et al. (2015).

The smaller SHs of the GCXE (see table 2) than those of CVs and ABs also support that GCXE needs large additional components with smaller SHs than CVs and ABs. One plausible site of the GCXE is the central molecular zone (CMZ) (Tsuboi et al. 1999; Wienen et al. 2015). Possible origin is a large amount of SNRs or very active star formation (Koyama et al. 1986) in the CMZ.

Another possibility is that the GCXE is due to the past high energy activities (flares of Sgr A*), which is responsible for the XRNe, a recombining plasma (Nakashima et al. 2013), the Fermi bubble (Su et al. 2010) and jet-like structures (Koyama et al. 2003; Muno et al. 2008; Heard & Warwick 2013b). All these possibilities can produce not only a HP responsible for the Fe XXV Heα and Fe XXVI Lyα lines but also non-thermal particles responsible for the Fe I Kα line (Nobukawa et al. 2015; Sato et al. 2015). The excess of the Fe I Kα, Fe XXV Heα and Fe XXVI Lyα lines in the Sgr A East region (Park et al. 2004; Koyama et al. 2007b) would be a good example.

The authors are grateful to all members of the Suzaku team. This work was supported by the Japan Society for the Promotion of Science (JSPS) KAKENHI (No24540232, SY; No24740123, MN; No24540229, KK). KKN is supported by Research Fellow of JSPS for Young Scientists.

References

Ak, T., Bilir, S., Ak, S., & Eker, Z. 2008, NewA, 13, 133

Antunes, A., Nagase, F., & White, N. E. 1994, ApJ, 436, L83

Audard, M., Güdel, M., Sres, A., Raassen, A. J. J., & Mewe, R. 2003, A&A, 398, 1137

Balucinska-Church, M., & McCammon, D. 1992, ApJ, 400, 699

Bernardini, F., de Martino, D., Falanga, M., Mukai, K., Matt, G., Bonnet-Bidaud, J. -M., Masetti, N., & Mouchet, M. 2012, A&A, 542, A22

Bimmey, J., & Tremaine, S. 2008, Galactic Dynamics (Second Eddition), Princeton University Press

Byckling, K., Mukai, K., Thorstensen, J. R., & Osborne, J. P. 2010, MNRAS, 408, 2298

Czesla, S., & Schmitt, J. H. M. M. 2010, A&A, 520, A38

Dempsey, R. C., Linsky, J. L., Schmitt, J. H. M. M., & Fleming, T. A. 1993, ApJ, 413. 333

Doyle, J. G., et al. 1991, MNRAS, 248, 503

Ebisawa, K., et al. 2005, ApJ, 635, 214

Ebisawa, K., et al. 2008, PASJ, 60, S223

Eze, R. N. C. 2015, Mem. S. A. It., 86, 96

Ezuka, H., & Ishida, M. 1999, ApJS, 120, 277

Gendreau, K. C., et al. 1995, PASJ, 47, L5

Gilmore, G. F., & Zeilik M. 2000, in Allen's Astrophysical Quantities, 4th ed., ed. A. N. Cox (New York, Springer), ch. 19

Güdel, M. 2004, A&A review, 12, 71

Güdel, M., Linsky, J. L., Brown, A., & Nagase, F. 1999, ApJ, 511, 405

Hawkins, M. R. S. 1988, MNRAS, 234, 533

Heard, V., & Warwick, R. S. 2013a, MNRAS, 428, 3462

Heard, V., & Warwick, R. S. 2013b, MNRAS, 434, 1339

Hellier, C., & Mukai, K. 2004, MNRAS, 352, 1037

Hellier, C., Mukai, K., & Osborne, J. P. 1998, MNRAS, 297, 526

Hong, J. 2012, MNRAS, 427, 1633

Imanishi, K., Nakajima, H., Tsujimoto, M., Koyama, K., & Tsuboi, Y. 2003, PASJ, 55, 653

Kaastra, J. S., & Mewe, R. 1993, A&AS, 97, 443

Kaneda, H., Makishima, K., Yamauchi, S., Koyama, K., Matsuzaki, K., & Yamasaki, N. Y. 1997, ApJ, 491, 638

Koyama, K., Makishima, K., Tanaka, Y., & Tsunemi, H. 1986, PASJ, 38, 121

Koyama, K., Awaki, H., Kunieda, H., Takano, S., Tawara, Y., Yamauchi, S., Hatsukade, I., & Nagase, F. 1989, Nature, 339, 603

Koyama, K., Maeda, Y., Sonobe, T., Takeshima, T., Tanaka, Y., & Yamauchi, S. 1996, PASJ, 48, 249

Koyama, K., Senda, A., Murakami, H., & Maeda, Y. 2003, ChJAS, 3, 297

Koyama, K., et al. 2007a, PASJ, 59, S23

Koyama, K., et al. 2007b, PASJ, 59, S245

Kushino, A., Ishisaki, Y., Morita, U., Yamasaki, N. Y., Ishida, M., Ohashi, T., & Ueda, Y. 2002, PASJ, 54, 327

Liu, Q. Z., van Paradijs, J., & van den Heuvel, E. P. J. 2007, A&A, 469, 807

Marshall, F. E., Boldt, E. A., Holt, S. S., Miller, R. B., Mushotsky, R. F., Rose, L. A., Rothschild, R. E., & Serlemitsos, P. J. 1980, ApJ, 235, 4

Mathis, J. S. 2000, in Allen's Astrophysical Quantities, 4th ed., ed. A. N. Cox (New York, Springer), ch. 21

Mitsuda, K., et al. 2007, PASJ, 59, S1

Molaro, M., Khatri, R., & Sunyaev, R. A. 2014, A&A, 564, 107

Morihana, K., Tsujimoto, M., Yoshida, T., & Ebisawa, K. 2013, ApJ, 766, 14

Mukai, K., & Shiokawa, K. 1993, ApJ, 418, 863

Muno, M. P., et al. 2003, ApJ, 589, 225

Muno, M. P., et al. 2004, ApJ, 613, 1179

Muno, M. P., Baganoff, F. K., Brandt, W. N., Morris, M. R., & Starck, J-. L. 2008, ApJ, 673, 251

Nakashima, S., et al. 2013, ApJ, 773, 20

Nobukawa, K. K., et al. 2015, ApJ, 807, L10

Osten, R. A., Brown, A., Ayres, T. R., Linsky, J. L., Drake, S. A., Gagné, M., & Stern, R. A. 2000, ApJ, 544, 953

Ozawa, H., Grosso N., & Montmerle, T. 2005, A&A, 429, 963

Pandey, J. C., & Singh, K. P. 2008, MNRAS, 387, 1627

Pandey, J. C., & Singh, K. P. 2012, MNRAS, 419, 1219

Park, S., Muno, M. P., Baganoff, F. K., Maeda, Y., Morris, M., Howard, C., Bautz, M. W., & Garmire, G. P. 2004, ApJ, 603, 548

Patterson, J. 1984, ApJS, 54, 443

Prisinzano, L., et al. 2008, ApJ, 677, 401

Rana, V. R., Singh, K. P., Schlegel, E. M., & Barrett, P. E. 2006, ApJ, 642, 1042

Revnivtsev, M., Gilfanov, M., Jahoda, K., & Sunyaev, R. 2005, A&A, 444, 381

Revnivtsev, M., Sazonov, S., Gilfanov, M., Churazov, E., & Sunyaev, R. 2006, A&A, 452, 169

Revnivtsev, M., Vikhlinin, A., & Sazonov, S. 2007, A&A, 473, 857

Revnivtsev, M., Sazonov, S., Krivonos, R., Ritter, H., & Sunyaev, R. 2008, A&A, 489, 1121

Revnivtsev, M., Sazonov, S., Churazov, E., Forman, W., Vikhlinin A., & Sunyaev, R. 2009, Nature, 458, 1142

Sato, T., Koyama, K., Takahashi, T., Odaka, H., & Nakashima, S. 2014, PASJ, 66, 124

Sato, T., Koyama, K., Lee, S. -H., & Takahashi, T. 2015, PASJ, accepted (arXiv.1512.04300)

Sazonov, S., Revnivtsev, M., Gilfanov, M., Churazov, E., & Sunyaev, R. 2006, A&A, 450, 117

Sakano, M., Koyama, K., Murakami, H., Maeda, Y., & Yamauchi, S. 2002, ApJS, 138, 19

Schmitt, J. H. M. M., Collura, A., Sciortino, S., Vaiana, G. S., Harnden, F. R. Jr., & Rosner, R. 1990, ApJ, 365, 704

Serlemitsos, P., et al. 2007, PASJ, 59, S9

Stark, A. A., & Lee, Y. , 2005, ApJ, 619, 159

Strassmeier, K. G., Hall, D. S., Fekel, F. C., & Scheck, M. 1993, A&AS, 100, 173

Su, M., Slatyer, T. R., & Finkbeiner, D. P. 2010, ApJ, 724, 1044

Sugizaki, M., Mitsuda, K., Kaneda, H., Matsuzaki, K., Yamauchi, S., & Koyama, K. 2001, ApJS, 134, 77

Takagi, S., Murakami, H., & Koyama, K. 2002, ApJ, 573, 275

Tawa, N., et al. 2008, PASJ, 60, S11

Tsuboi, M., Handa, T., & Ukita, N. 1999, ApJS, 120, 1

Tsujimoto, M., Feigelson, E. D., Grosso, N., Micela, G., Tsuboi, Y., Favata, F., Shang, H., & Kastner, J. H. 2005, ApJS, 160, 503

Tsuru, T., et al. 1989, PASJ, 41, 679

Uchiyama, H., Nobukawa, M., Tsuru, T. G., Koyama, K., & Matsumoto, H. 2011, PASJ, 63, S903

Uchiyama, H., Nobukawa, M., Tsuru, T. G., & Koyama, K. 2013, PASJ, 65, 19

Warwick, R. S., Turner, M. J. L., Watson, M. G., & Willingale, R. 1985, Nature, 317, 218

Warwick, R. S., Byckling, K., & Pérez-Ramírez, D. 2014, MNRAS, 438, 2967

White, N. E., et al. 1994, PASJ, 46, L97

Wienen, M., et al. 2015, A&A, 579, 91

Worrall, D. M., Marshall, F. E., Boldt, E. A., & Swank, J. H. 1982, ApJ, 255, 111

Xu, X.-J., Wang, Q. D., & Li, X.-D. 2016, ApJ, 818, 136

Yamauchi, S., Kawada, M., Koyama, K., Kunieda, H., Tawara, Y., & Hatsukade, I. 1990, ApJ, 365, 532

Yamauchi, S., & Koyama, K. 1993, ApJ, 404, 620

Yamauchi, S., Ebisawa, K., Tanaka, Y., Koyama, K., Matsumoto, H., Yamasaki, N. Y., Takahashi, H., & Ezoe, Y. 2009, PASJ, 61, S225

Yasui, K., et al. 2015, PASJ, 67, 123

Yasumi, M., Nobukawa, M., Nakasihma, S., Uchida, H., Sugawara, R., Tsuru, T. G., Tanaka, T., & Koyama, K. 2014, PASJ, 66, 68

Table 1. Observation logs.

Sequence No.	Pointing position	Observation time (UT)	Exposure
	l, b	Start – End	(ksec)
407094010	322.06, −0.42	2012-08-15 15:34:02 – 2012-08-16 00:11:17	30.0
501043010	330.40, −0.38	2006-09-16 11:02:03 – 2006-09-17 07:14:14	43.6
503073010	331.30, −0.76	2008-09-20 18:18:35 – 2008-09-21 13:30:14	53.7
503074010	331.47, −0.64	2008-09-21 13:31:03 – 2008-09-22 06:40:12	52.6
501042010	331.57, −0.53	2006-09-15 16:00:48 – 2006-09-16 10:58:14	40.2
100028020	332.00, −0.15	2005-09-18 22:47:36 – 2005-09-19 11:58:41	19.3
100028010	332.40, −0.15	2005-09-19 12:00:02 – 2005-09-20 19:38:24	41.4
100028030	332.70, −0.15	2005-09-20 19:40:17 – 2005-09-21 07:29:24	21.9
401056010	333.54, 0.33	2006-09-20 20:25:12 – 2006-09-21 17:21:20	39.1
407018010	333.61, −0.20	2012-08-21 23:55:27 – 2012-08-22 22:33:20	40.5
407020010	333.72, 0.22	2012-08-19 12:30:06 – 2012-08-20 12:35:23	44.3
407091010	333.89, 0.41	2012-08-18 19:16:15 – 2012-08-19 12:29:17	29.3
507068010	337.21, −0.73	2012-09-02 13:16:23 – 2012-09-11 06:14:09	304.2
404056010	338.00, 0.08	2010-03-12 23:40:40 – 2010-03-14 10:49:14	50.6
505049010	339.01, −0.93	2010-09-10 18:33:35 – 2010-09-12 04:50:16	51.9
505051010	339.43, −0.80	2010-09-23 06:09:00 – 2010-09-24 09:28:16	50.2
505050010	339.79, −1.14	2010-09-12 04:52:53 – 2010-09-13 14:35:12	52.7
401052010	340.05, 0.13	2006-09-09 09:12:56 – 2006-09-09 22:05:14	22.5
406078010	340.17, −0.12	2012-02-23 22:39:06 – 2012-02-26 12:52:21	149.8
405027010	340.44, −0.18	2011-02-11 03:42:23 – 2011-02-11 18:16:19	20.9
505052010	340.77, −1.01	2010-09-24 09:32:21 – 2010-09-25 12:29:19	49.6
401054010	341.37, 0.60	2006-10-05 21:10:30 – 2006-10-06 10:05:24	21.1
502049010	344.26, −0.22	2008-03-25 11:00:23 – 2008-03-30 15:00:14	215.7
100026030	345.80, −0.54	2005-09-28 07:09:13 – 2005-09-29 04:25:24	37.5
100026020	347.63, 0.71	2005-09-25 19:11:40 – 2005-09-26 15:42:09	34.9
505076010	347.85, −0.23	2011-02-16 01:17:29 – 2011-02-16 23:10:11	32.6
501105010	348.80, −0.54	2007-02-23 08:36:38 – 2007-02-23 18:39:24	20.7
503108010	348.92, −0.45	2008-08-28 05:36:23 – 2008-08-28 22:17:14	23.5
408021010	352.17, −0.27	2013-09-05 00:04:43 – 2013-09-05 19:14:14	37.3
405026010	355.27, 0.39	2011-02-19 23:54:57 – 2011-02-20 16:43:24	20.9

Table 1. (Continued)

Sequence No.	Pointing position l, b	Observation time (UT) Start – End	Exposure (ksec)
503022010	356.00, 0.70	2009-03-18 23:11:24 – 2009-03-19 21:26:24	41.3
504049010	356.30, 1.00	2009-09-08 03:36:55 – 2009-09-09 02:36:11	18.2
503023010	356.33, 0.70	2009-03-26 06:37:01 – 2009-03-27 01:53:19	31.2
503020010	356.40, −0.05	2009-02-21 01:15:55 – 2009-02-22 18:59:14	61.1
505082010	356.40, −0.40	2011-03-15 13:54:28 – 2011-03-16 14:54:23	48.5
505083010	356.40, −0.80	2010-10-10 14:04:38 – 2010-10-11 21:33:13	52.9
505084010	356.40, −1.50	2011-03-06 05:36:44 – 2011-03-07 13:01:11	50.3
505085010	356.40, −2.30	2010-10-13 06:04:47 – 2010-10-14 13:30:17	55.0
505086010	356.40, −3.50	2010-10-14 13:31:50 – 2010-10-16 01:30:25	54.1
503019010	356.65, −0.05	2009-02-19 16:37:49 – 2009-02-21 01:15:14	52.8
503018010	356.90, −0.05	2008-09-24 09:27:54 – 2008-09-24 22:30:24	29.4
503018020	356.90, −0.05	2008-10-03 18:05:13 – 2008-10-04 03:42:18	12.2
503018030	356.90, −0.05	2009-02-19 07:32:01 – 2009-02-19 16:36:24	11.9
503017010	357.15, −0.05	2008-09-23 08:08:10 – 2008-09-24 09:21:13	51.3
503016010	357.40, −0.05	2008-09-22 06:47:49 – 2008-09-23 08:07:17	52.2
503015010	357.65, −0.05	2008-09-19 07:33:05 – 2008-09-20 09:56:13	56.8
504036010	357.71, −0.12	2009-08-29 12:05:20 – 2009-09-01 00:13:24	136.5
503014010	357.90, −0.05	2008-09-18 04:46:49 – 2008-09-19 07:32:20	55.4
501053010	358.17, 0.00	2006-10-10 21:18:59 – 2006-10-11 10:06:14	21.9
504002010	358.47, −0.59	2010-02-27 16:14:41 – 2010-02-28 22:50:14	53.1
501052010	358.50, 0.00	2006-10-10 06:45:09 – 2006-10-10 21:18:14	19.3
504090010	358.50, −1.20	2009-10-13 04:17:20 – 2009-10-14 11:29:06	52.9
504091010	358.50, −1.60	2009-09-14 19:37:36 – 2009-09-16 07:18:14	51.3
504092010	358.50, −2.15	2009-09-16 07:21:35 – 2009-09-17 13:49:14	50.9
504093010	358.50, −2.80	2009-09-17 13:54:31 – 2009-09-19 03:37:14	53.2
504094010	358.50, −3.80	2009-09-19 03:40:31 – 2009-09-21 14:33:19	93.1
504095010	358.50, −5.00	2009-10-15 15:32:28 – 2009-10-16 18:00:19	48.3
504001010	358.53, −0.27	2010-02-26 09:15:00 – 2010-02-27 16:13:16	51.2
504003010	358.55, −0.87	2010-02-25 04:33:17 – 2010-02-26 09:13:19	50.9
501051010	358.83, 0.00	2006-10-09 13:40:09 – 2006-10-10 06:44:24	21.9
500019010	358.91, −0.04	2006-02-23 10:51:11 – 2006-02-23 20:02:19	13.3

Table 1. (Continued)

Sequence No.	Pointing position l, b	Observation time (UT) Start – End	Exposure (ksec)
500018010	359.43, −0.09	2006-02-20 12:45:25 – 2006-02-23 10:50:14	106.9
503072010	359.58, 0.17	2009-03-06 02:39:12 – 2009-03-09 02:55:25	140.6
100027020	359.75, −0.05	2005-09-24 14:17:17 – 2005-09-25 17:27:19	42.8
100037010	359.75, −0.05	2005-09-29 04:35:41 – 2005-09-30 04:29:19	43.7
503099010	359.78, 1.13	2009-03-10 19:39:08 – 2009-03-11 10:56:14	29.7
502008010	359.83, 0.67	2007-10-12 09:52:59 – 2007-10-12 21:50:19	23.8
501046010	359.83, 0.33	2007-03-10 15:03:10 – 2007-03-11 03:55:14	25.2
502003010	359.83, −0.67	2007-10-10 03:41:13 – 2007-10-10 15:20:24	21.5
502005010	359.83, −1.00	2007-10-11 01:01:17 – 2007-10-11 11:32:20	20.6
501008010	359.85, −0.19	2006-09-26 14:18:16 – 2006-09-29 21:25:14	129.6
501009010	359.93, 0.18	2006-09-29 21:26:07 – 2006-10-01 06:55:19	51.2
504089010	359.95, −1.20	2009-10-09 04:05:59 – 2009-10-10 14:10:06	55.3
505079010	359.95, −2.80	2011-03-12 06:36:20 – 2011-03-13 10:17:21	50.2
505080010	359.95, −3.80	2010-04-07 17:15:10 – 2010-04-09 21:14:16	56.1
503103010	359.99, 1.20	2009-03-11 10:56:59 – 2009-03-11 19:17:08	18.3
503008010	0.00, −0.38	2008-09-03 22:53:29 – 2008-09-05 06:56:19	53.7
504088010	0.00, −0.83	2009-10-14 11:30:56 – 2009-10-15 15:29:19	47.2
502059010	0.00, −2.00	2007-09-29 01:40:51 – 2007-10-02 14:10:16	136.8
503081010	0.04, −1.66	2009-03-09 15:41:50 – 2009-03-10 19:36:19	59.2
100027010	0.06, −0.07	2005-09-23 07:18:25 – 2005-09-24 11:05:19	44.8
100037040	0.06, −0.07	2005-09-30 07:43:01 – 2005-10-01 06:21:24	43
504050010	0.10, −1.42	2010-03-06 03:55:37 – 2010-03-08 21:26:19	100.4
502007010	0.17, 0.67	2007-10-11 23:09:15 – 2007-10-12 09:52:14	22.0
502006010	0.17, 0.33	2007-10-11 11:34:01 – 2007-10-11 23:07:14	22.6
502002010	0.17, −0.67	2007-10-09 16:40:54 – 2007-10-10 03:40:24	23.2
502004010	0.17, −1.00	2007-10-10 15:21:17 – 2007-10-11 01:00:24	19.9
502022010	0.23, −0.27	2007-08-31 12:33:33 – 2007-09-03 19:00:25	134.8
503007010	0.33, 0.17	2008-09-02 10:15:27 – 2008-09-03 22:52:24	52.2
500005010	0.43, −0.12	2006-03-27 23:00:22 – 2006-03-29 18:12:15	88.4
100037060	0.64, −0.10	2005-10-10 12:28:01 – 2005-10-12 07:05:23	76.6
100037070	1.00, −0.10	2005-10-12 07:10:24 – 2005-10-12 11:05:24	9.2

Table 1. (Continued)

Sequence No.	Pointing position	Observation time (UT)	Exposure
	l, *b*	Start – End	(ksec)
501059010	1.17, 0.00	2007-03-15 18:55:51 – 2007-03-17 05:06:19	62.2
501058010	1.30, 0.20	2007-03-14 05:02:29 – 2007-03-15 18:55:14	63.3
501060010	1.50, 0.00	2007-03-17 05:07:04 – 2007-03-18 20:58:14	64.8
508075010	1.75, −0.04	2014-03-10 01:33:32 – 2014-03-12 15:30:12	109.3
502009010	1.83, 0.00	2007-10-12 21:52:24 – 2007-10-13 07:30:19	20.9
505053010	1.87, 0.32	2011-03-23 03:51:35 – 2011-03-25 06:51:20	100.9
507069010	2.00, −0.04	2013-03-15 09:48:19 – 2013-03-17 18:39:15	110.3
507070010	2.25, −0.04	2013-03-17 18:39:56 – 2013-03-20 02:40:03	111.8
507071010	2.50, −0.04	2013-03-20 02:41:04 – 2013-03-22 07:19:07	112.3
507072010	2.75, −0.04	2013-03-22 07:20:36 – 2013-03-24 08:45:10	110.7
507073010	3.00, −0.04	2013-03-24 08:46:03 – 2013-03-26 09:53:12	108.9
508076010	3.25, −0.04	2014-02-28 12:46:16 – 2014-03-02 17:00:14	109.8
508077010	3.50, −0.04	2014-03-02 17:00:51 – 2014-03-04 23:00:15	109.4
503027010	5.72, −0.06	2008-04-07 00:21:13 – 2008-04-07 16:30:23	31.0
503026010	5.89, −0.38	2008-04-06 07:34:41 – 2008-04-07 00:20:24	31.7
500008010	8.04, −0.05	2006-04-07 11:49:16 – 2006-04-08 10:54:18	40.7
407092010	8.14, 0.19	2012-09-21 08:05:31 – 2012-09-22 04:09:13	32.0
500007010	8.44, −0.05	2006-04-06 14:41:18 – 2006-04-07 11:48:23	37.5
401092010	9.94, −0.27	2006-09-09 22:13:43 – 2006-09-11 04:00:14	48.9
402094010	9.95, −0.27	2007-10-14 05:35:49 – 2007-10-15 08:00:23	52.2
406069010	10.00, −0.23	2012-03-24 10:47:46 – 2012-03-26 12:45:20	70.6
504079010	10.72, 0.33	2009-09-11 17:59:44 – 2009-09-13 03:45:16	51.0
503079010	10.84, 0.04	2008-04-01 16:33:52 – 2008-04-02 14:47:18	44.2
503078010	11.03, 0.07	2008-03-31 14:05:55 – 2008-04-01 16:30:23	51.5
504078010	11.33, −0.06	2009-09-10 11:36:47 – 2009-09-11 17:58:19	52.5
504077010	11.61, −0.25	2009-09-09 04:55:29 – 2009-09-10 11:35:14	51.9
502001010	11.95, −0.09	2007-10-02 14:17:21 – 2007-10-03 23:40:19	53.8
503087010	12.82, −0.02	2009-03-04 19:45:39 – 2009-03-06 02:31:19	56.2
401101010	12.87, 0.01	2007-03-01 21:35:58 – 2007-03-03 06:45:19	63.8
502053010	15.82, −0.84	2007-10-07 02:16:29 – 2007-10-08 18:10:14	71.5
503030010	17.47, −0.58	2008-10-19 04:41:55 – 2008-10-20 19:00:07	55.5

Table 1. (Continued)

Sequence No.	Pointing position	Observation time (UT)	Exposure
	l, b	Start – End	(ksec)
503028010	17.61, −0.84	2008-10-15 21:49:50 – 2008-10-17 11:00:23	57.2
503029010	17.73, −0.44	2008-10-17 11:01:12 – 2008-10-19 04:41:14	57.2
501044010	17.87, −0.70	2006-10-17 19:37:16 – 2006-10-19 04:02:15	50.3
503086010	18.00, −0.69	2009-03-19 21:33:25 – 2009-03-21 01:56:19	52.1
501045010	18.44, −0.84	2006-10-19 04:03:16 – 2006-10-20 12:10:25	52.2
506051010	18.78, 0.40	2012-03-08 22:01:58 – 2012-03-10 03:50:15	52.0
507044010	19.57, 0.01	2012-10-15 13:05:48 – 2012-10-19 17:57:06	171.8
505025010	22.00, 0.00	2010-04-16 14:27:26 – 2010-04-17 17:27:12	50.5
506021010	23.29, 0.30	2011-04-08 06:06:16 – 2011-04-09 08:17:25	40.3
904006010	23.40, 0.04	2010-03-27 09:03:32 – 2010-03-28 11:37:12	42.3
505026010	23.49, 0.04	2010-10-20 13:34:39 – 2010-10-22 01:45:11	49.0
401026010	25.21, −0.12	2007-03-05 12:49:14 – 2007-03-06 10:17:14	42.2
504099010	25.50, 0.00	2009-04-06 02:57:46 – 2009-04-07 17:52:14	52.7
505088010	26.30, 0.00	2011-03-25 07:00:01 – 2011-03-26 10:40:15	49.7
505089010	26.40, −0.31	2011-03-26 10:41:12 – 2011-03-27 15:20:23	50.0
504052010	26.44, 0.13	2009-04-13 15:32:05 – 2009-04-14 18:11:19	41.1
505090010	26.71, −0.15	2011-03-27 15:21:16 – 2011-03-28 19:00:18	49.6
505091010	27.13, −0.28	2011-03-28 19:01:23 – 2011-03-29 23:07:13	51.3
500009010	28.46, −0.20	2005-10-28 02:40:08 – 2005-10-30 21:30:15	93.3
500009020	28.46, −0.20	2006-10-15 02:15:12 – 2006-10-17 19:32:19	98.9
404081010	29.71, −0.24	2009-04-15 19:37:17 – 2009-04-18 16:16:14	104.3
508022010	35.61, −0.40	2013-10-28 23:25:55 – 2013-10-30 03:09:09	52.6
506019010	36.00, 0.05	2011-09-18 22:04:29 – 2011-09-19 23:37:16	40.9
505027010	37.00, −0.10	2010-04-17 17:35:13 – 2010-04-18 21:09:18	51.0
509038010	39.19, −0.30	2014-04-26 06:42:08 – 2014-04-28 02:56:13	82.8

Table 2. Best-fit parameters of the GCXE, GBXE and GRXE.

Region	Component	Parameter				
		Normalization (A^*)			e-folding scale ($b^\dagger$)	Scale height‡
		l=0°	l=358.°5	l=356.°0–356.°4		
GCXE	6.4 keV	4.1±0.2	= $A_{l=0^\circ}$ ×0.11	= $A_{l=0^\circ}$ ×0.004	0.22±0.02	31±3
	6.7 keV	11.9±0.6	= $A_{l=0^\circ}$ ×0.11	= $A_{l=0^\circ}$ ×0.004	0.26±0.02	36±3
	6.97 keV	4.9±0.2	= $A_{l=0^\circ}$ ×0.11	= $A_{l=0^\circ}$ ×0.004	0.24±0.02	34±3
	5–8 keV	77±4	= $A_{l=0^\circ}$ ×0.11	= $A_{l=0^\circ}$ ×0.004	0.25±0.02	35±3
GBXE	6.4 keV	0.31±0.15	0.35±0.10	0.28±0.07	1.15±0.36	161±50
	6.7 keV	1.14±0.34	1.15±0.27	1.04±0.21	2.25±0.68	314±95
	6.97 keV	0.40±0.12	0.39±0.10	0.19±0.06	2.13±0.66	297±92
	5–8 keV	12±2	10.6±1.4	7.2±0.9	1.96±0.25	274±35
		l=10°–30°	l=330°–350°			
GRXE	6.4 keV	0.23±0.03	0.28±0.04		0.50±0.12	70±17
	6.7 keV	0.76±0.02	0.54±0.03		1.02±0.12	142±17
	6.97 keV	0.09±0.02	= $A_{l=10^\circ-30^\circ}$		0.71±0.29	99±40
	5–8 keV	5.8±0.4	4.9±0.5		1.04±0.20	145±28

Error is 1 σ (68% confidence) level.

$*$: Unit is 10^{-7} photons s^{-1} cm^{-2} $arcmin^{-2}$.

†: Unit is degree.

‡: Unit is pc. Distance of 8 kpc is assumed.

Table 3. Equivalent width of mCVs, nmCVs and ABs

Sources	$EW_{6.4}$ (eV)	$EW_{6.7}$+$EW_{6.97}$ (eV)	Luminosity (erg s^{-1})
mCVs	∼120	∼260	∼ 10^{32}–10^{34}
nmCVs	∼70	∼530	∼ 10^{30}–10^{32}
ABs (& CAs)	≤20	300–650	∼ 10^{27}–10^{32}
GCXE	145±3	748±5	
GBXE	61±11	603±20	
GRXE	97±12	545±24	

Error is 1 σ (68% confidence) level.